

Multifunctional Films Deposited by Atomic Layer Deposition for Tailored Interfaces of Electrochemical Systems

To cite this article: Arturo Gutierrez et al 2020 J. Electrochem. Soc. 167 140541

View the <u>article online</u> for updates and enhancements.





Multifunctional Films Deposited by Atomic Layer Deposition for Tailored Interfaces of Electrochemical Systems

Arturo Gutierrez,^{1,=} Devika Choudhury,^{2,=} Soroosh Sharifi-Asl,³ Bryan T. Yonemoto,¹ Reza Shahbazian-Yassar,³ Anil U. Mane,^{2,*} Jeffrey W. Elam,^{2,*} and Jason Croy^{1,z}

A new strategy for electrochemical interfaces that utilizes multilayer films deposited by atomic layer deposition (ALD) is introduced. Manganese-rich and nickel-rich cathode oxides were coated with a novel bilayer film of metal fluorides. Subsequent exposure to prolonged, high-voltage electrochemical cycling vs graphite electrodes revealed that the bilayer film can greatly enhance the high-voltage stability of cathode oxides. In particular, in manganese-rich cells, capacity fade due to manganese dissolution was substantially reduced and impedance rise was virtually eliminated. Furthermore, in nickel-rich NMC-811 cells, impedance rise was reduced by \sim 80%, compared to the NMC-811 baseline, after \sim 300 h of high-voltage exposure during cycling. The multilayer film strategy presents an exciting opportunity for tailoring designs and materials for electrochemical interfaces in advanced lithium-ion batteries and beyond.

© 2020 The Electrochemical Society ("ECS"). Published on behalf of ECS by IOP Publishing Limited. [DOI: 10.1149/1945-7111/abc768]

Manuscript submitted August 21, 2020; revised manuscript received October 6, 2020. Published November 16, 2020.

Supplementary material for this article is available online

The growing demand for next-generation lithium-ion batteries (LIBs) is driven largely by the push to electrify the transportation sector (i.e., electric vehicles [EVs]). To help achieve this goal, the Vehicle Technologies Office of the U.S. Department of Energy has set a goal to reduce the cost of EV batteries from the current ~\$235 kWh⁻¹ to \$100 kWh⁻¹ (pack-level cost). The current state-of-theart LIB is based on a transition metal-oxide cathode (LMeO, Me=Mn, Ni, Co, Al) paired against a graphite-based anode (LMO//graphite). Currently, the conventional cathodes deliver a specific energy of 700-800 Wh/kg_{oxide} (vs Li⁰/Li⁺). However, the specific energy target range for cathodes to help meet the target cost is 800–1000 Wh/kg_{oxide} (vs Li⁰/Li⁺). Lithium- and manganese-rich (LMR) cathode materials with composition $xLi_2MnO_3 \cdot (1-x)LiMO_2$, also called layered-layered (LL) composites, are strong candidates to meet these demands because of their high gravimetric capacities $(250-300 \text{ mAh g}^{-1})^{2-4}$ and the low cost of manganese compared to other commonly used transition metals, such as cobalt and nickel. In addition, while the challenges of voltage fade and hysteresis⁵ are often cited as mitigating factors, several strategies have shown success in advancing these materials towards practical viability including optimized Li:Mn:TM contents,⁶ tailored voltage windows,^{6,7} and modifications to local structures of the bulk and surface, as presented herein as well as in Refs. 8-10. At present, issues related to impedance rise, Mn dissolution, and capacity fade with cycling, specifically in graphite cells, are a major hindrance to future success. As such, if new paths forward can be found in this regard, LMR cathodes represent very attractive, sustainable materials for next-gen oxides.

As with all cathode oxides, the cycling (in)stability at high states of charge (SOCs) is greatly determined by surface reactivity. This is especially true in the sense that the most desirable LMR compositions are those that are richest in manganese (~50% or more). Dissolution of manganese into electrolytes and subsequent migration and deposition at graphitic anodes is now a well-known mechanism of capacity fade in most all conventional, manganese-containing cathode oxides. As such, it is imperative to the development of these materials that strategies be identified that enable robust surfaces and

surface structures that are resistant to metal etching and reconstruc-

The literature identifies many coating strategies that improve the surface stability of transition metal oxides used in LIBs. The approaches range in chemistry from phosphates to oxides to carbons. Many of the results presented are promising, but several concerns and challenges remain. First, many studies only present data of coated cathodes when cycled against Li metal anodes. The virtually infinite supply of Li ions in such cells often masks any deficiencies in the coatings by concealing the effects of active lithium loss due to crosstalk in the cell. In addition, most wet-chemical treatments (and subsequent heating processes) can serve to cleanse the cathode oxide surface of unwanted/unreacted residues on the oxide. It is wellknown that a "clean" cathode surface leads to better performance. In addition, very little data related to practical cycling exists where cells are exposed to various rates or long periods of high voltage. Since high SOCs are the most critical in terms of mitigating surface degradation, exposure to such SOCs during the evaluation of surface treatments is crucial.

Also of concern with most processing techniques is lack of uniformity and thickness in the coating materials. Atomic layer deposition (ALD) is interesting in this regard as it allows for (1) atomic-level control of coating thickness, (2) conformal coverage of a contoured surface, (3) low-temperature deposition, and (4) high reproducibility. In addition, the versatility of the method allows for the synthesis of a wide range of chemistries, and its proven ability to be scaled has led to its implementation in industry. ¹¹

Metal oxides like Al₂O₃, TiO₂, ZrO₂, and MgO are well-established ALD coatings used on various electrodes, including LiCoO₂, ^{12,13} Ni-rich nickel-manganese-cobalt (NMC) cells, ^{14–16} and even LMR cathodes. ^{17,18} Although metal-oxide ALD coatings show improved performance in the reported literature, they are considered to be thermodynamically unstable within the "normal" operating voltage used for cycling. ¹⁹ This innate instability makes them prone to anodic decomposition during continuous operation in the battery. Metal fluorides, on the other hand, characteristically possess excellent stability in a wide voltage window, while also displaying limited reactivity toward the cathode and/or the electrolyte, ^{19,20} which ensures metal-fluoride coatings remain passive during battery operation. Yet, the low ionic conductivity inherent to metal fluorides needs to be overcome for efficient charge transfer to occur across the electrolyte//coating//cathode interfaces. One successful way to

¹Chemical Sciences and Engineering Division, Argonne National Laboratory, Lemont, Illinois 60439, United States of America

²Applied Materials Division, Argonne National Laboratory, Lemont, Illinois 60439, United States of America

³ Mechanical and Industrial Engineering Department, University of Illinois at Chicago, Chicago, Illinois 60607, United States of America

⁼These authors contributed equally to this work.

^{*}Electrochemical Society Member.

^zE-mail: croy@anl.gov

improve the ionic conductivity of metal-fluoride (i.e., LiF) thin films is through the addition of aliovalent cations to the composition (e.g., LiAlF₄). More recently, LiAlF₄ was successfully applied to LiNi_{0.8}Mn_{0.1}Co_{0.1}O₂ through ALD and shown to improve the cycle-life performance and impedance properties. Our own group has previously reported on a composite AlW_xF_y coating that incorporates aliovalent doping (i.e., W^{δ +}) into the parent metal fluoride (AlF₃) on LiCoO₂ electrodes. The overall properties of the coated electrode were improved when compared to the untreated LiCoO₂. Therefore, it is of interest to test the effectiveness of this metal-fluoride coating on other cathode oxides, including LMR-based electrodes for which Mn dissolution from the oxide surface is a major concern.

Herein, we report on a strategy that utilizes multi-layer/component films deposited by ALD. The wide range of chemical precursors available, the flexibility of deposition, and the adaptability to industrial processing (high-throughput reactors and roll-to-roll fabrication) make ALD an attractive route forward in the design of advanced electrode materials for Li-ion and beyond. This strategy allows electrode/film, film/film, and film/electrolyte interfaces to be tailored via novel materials to create robust surfaces while allowing for facile lithium diffusion. Here we present results for a class of simple, but novel, bilayer metal-fluoride coatings, AlW_xF_y/AlF₃, applied to Mn-rich, layered-layered spinel (LLS) electrodes and tested under standardized, full-cell protocols. This pairing was chosen because AlW_xF_y has been shown to improve conductivity over AlF₃ deposited on cathode surfaces,²² while AlF₃, which is more chemically resistant, can create a robust interface with acidic electrolytes. The effectiveness of the bilayer coating to protect the underlying cathode was tested in cells containing graphite-based anodes; both the cathode and anode were analyzed following the tests.

Experimental

Synthesis of layered-layered spinel electrodes.—Layeredlayered spinel electrode materials were synthesized using NMC carbonate precursors with Mn_{0.53}Ni_{0.28}Co_{0.19}CO₃ composition. The NMC carbonates were prepared using a 4L continuously stirred tank reactor as follows. The tank was filled with an initial volume of 3L and then sealed. To reduce unwanted oxidation of the product, N₂ was allowed to flow through the tank to remove air from the water and headspace before the reaction was started. The stirring speed, temperature, and pH were controlled at 1000 RPM, 35 °C, and 8.3, respectively, for the remainder of the reaction. Solutions of 2 M NMC sulfates, 2 M sodium carbonate (Na₂CO₃ for pH control), and 0.05 M ammonium hydroxide (NH₄OH) were pumped into the reactor, allowing for a 6-h residence time. The product was collected after four residence times (24 h), then washed and dried under nitrogen gas at 130 °C. The dried transition metal carbonate was then mixed with lithium carbonate (Li₂CO₃) and fired at 900 °C for 20 h in air, followed by natural cooling in the furnace.

X-ray diffraction.—High-resolution synchrotron powder diffraction (HRXRD) data were collected using beamline 11-BM-B at the Advanced Photon Source, Argonne National Laboratory, using an average wavelength of 0.41 Å. Discrete detectors covering an angular range from -6 to 16° 2θ were scanned over a 34° 2θ range, with data points collected every 0.001° 2θ and scan speed of 0.01° s⁻¹. More details concerning the 11-BM-B instrument are provided in the Supporting Information.

Atomic layer deposition.—Atomic layer deposition of AlW_xF_y was carried out using trimethylaluminum (TMA, Strem Chemicals, USA) and tungsten hexafluoride (WF₆, Sigma-Aldrich, USA), while AlF₃ was deposited using TMA and hydrogen fluoride (HF)-pyridine (Sigma Aldrich, USA) precursors. All depositions were carried out in a custom-built ALD reactor on electrode laminates at a temperature of 150 °C under inert nitrogen atmosphere. All reactants

were kept at room temperature because of their sufficiently high vapor pressures and were pulsed into the reactor through differentially heated lines and pneumatically controlled valves. Layers of $\mathrm{AlW}_x\mathrm{F}_y$ were deposited using a dosing sequence of 2-30-2-30 s, where the 2 s is the dose time for both TMA and WF₆ and the 30 s is purging with nitrogen gas. For the AlF₃ layer, a 2-s dose time was again used for TMA, while a 4-s dose time was used for the HF-pyridine to obtain a saturated condition. The dosing sequence for AlF₃ was thus 2-30-4-30 s. A base pressure of 1 Torr (measured by a capacitance manometer, Baratron) was maintained during all depositions, with a flow of 225 sccm of nitrogen carrier gas controlled by mass flow controllers.

Transmission electron microscopy.—Particles were scraped from the current collector, sonicated, drop-cast onto lacy carbon grids, dried, and loaded on a double-tilt transmission electron microscope (TEM) holder. Scanning transmission electron microscopy (STEM) and electron energy loss spectroscopy (EELS) were performed using a cold field emission gun JEOL JEM-ARM200CF STEM with 0.78-Å spatial resolution, equipped with a Gatan Quantom EELS detector. A 22-mrad probe convergence angle was used to perform STEM imaging. A high-angle annular dark-field (HAADF) detector with 90-mrad inner-detector angle was utilized to obtain Z-contrast atomic resolution images. Electron dispersive spectroscopy (EDS) was carried out using an Oxford X-max 100TLE windowless silicon drift detector (SDD) X-ray detector.

Electrochemical characterization.—A slurry of the baseline LLS, polyvinylidene fluoride, and C45 carbon (84:8:8) was cast on aluminum foil to prepare electrodes. Graphite (\sim 92%) mixed with conductive carbon was used as the anode. All electrodes were dried in a vacuum oven overnight before cells were assembled in an argon-filled glovebox where the moisture and oxygen contents are controlled near or below 1 ppm. The N:P ratio was kept between 1.1 and 1.15 to ensure the capacity was always cathode-limited. On average the loading of the cathode was \sim 8 mg cm $^{-2}$. A polypropylene separator (Celgard 2325) was used in all cells. The electrolyte was 1.2 M LiPF₆ in ethylene carbonate: ethyl methyl carbonate (EC: EMC was 3:7 by weight).

Details about the cycling protocol can be found in Ref. 24. All cycling was carried out with 2032-type coin-cells in temperature controlled (30 $^{\circ}$ C) chambers. Briefly, the protocol consists of the following elements:

- A **formation cycle,** which allows for the wetting of electrodes and formation of the solid-electrolyte interphase on graphite. This formation cycle is only done once at the beginning of each test protocol. The first cycle includes an activation between 4.5 and 2.0 V (vs graphite) at C/10. All following cycles are carried out between 4.4 and 2.5 V.
- Hybrid-pulse-power-characterization (HPPC) preparation cycles, for three purposes:

To inspect the voltage profile under low current (C/10) during discharge to reduce the effects of impedance.

To probe the effect of a high current (1C) on the capacity during discharge (one cycle).

To gather information about the impedance as a function of the SOC of the cell.

• Aging cycles, used to accelerate the degradation of the cells by using a 3-h hold at the top of charge (4.4 V). These cycles are carried out using a current that allows a full discharge in 3 h (C/3).

The NMC electrodes were prepared by the Cell Analysis, Modeling and Prototyping (CAMP) facility at Argonne with cathode active material, polyvinylidene fluoride, and C45 carbon (90:5:5). The same electrolyte formulation and separator were used as given above. The average loading of the oxide was \sim 8.2 mg cm⁻². The

NMC electrodes were cycled using the same protocol described above except the upper and lower cutoff voltages were 4.3 and 3.0 V, respectively.

Results and Discussion

Initial characterization of baseline cathode powder.—The baseline cathode material used in this study was an LLS composite. As reported previously, the LLS is synthesized by using less lithium than the parent LL composite. For instance, the parent LL for this has a Li/transition metal ratio of 1.25 $0.25Li_2MnO_3 \cdot 0.75LiMn_{0.375}Ni_{0.375}Co_{0.25}O_2$). Therefore, achieving any Li/transition metal ratio below 1.25 during the initial calcination of the transition metal carbonate and lithium carbonate mixture generates an "underlithiated" component, leading to spinel-type local configurations in the composite material. A characterization of the resulting powder revealed the underlying chemistry and structure of the baseline cathode material. The nominal amount of spinel achieved in the baseline LLS used in this study is \sim 6%, on the basis of compositional analysis (Li_{1.18}Mn_{0.53}Ni_{0.28}Co_{0.19}O_{2.355}) conducted using inductively coupled plasma optical emission spectrometry. HRXRD was collected on the baseline material (Fig. S1a is available online at stacks.iop.org/JES/167/140541/mmedia). All main peaks can be indexed to space group R-3m with the exception of the C2/m ordering peaks at $\sim 2^{\circ}-3^{\circ} 2\theta$ (inset, Fig. S1a). The presence of integrated spinel domains at the surface was confirmed by TEM analysis (Figs. S1b-S1d), consistent with intentional "underlithiation" in the synthesis of LLS materials. Lastly, scanning electron microscope (SEM) images were collected on the baseline material, which revealed micron-sized, spherical secondary particles made up of nanometer-sized primary particles (Fig. S2).

TEM analysis of ALD coated samples.—The thickness of the first ALD layer (1 nm of AlW_xF_y) in the bilayer coating was fixed for all coated samples by using the film deposition rate previously reported.²² Since AlF₃ is known to be insulating and may have detrimental effects to the electrochemical performance (e.g., lower capacity and/or higher impedance), the thickness of the second layer (AlF₃), known to have a growth rate of 1 Å cycle⁻¹ at 150 °C, ²⁵ was varied between 0.4 and 1.5 nm by modifying the number of deposition cycles (4, 8, and 16 cycles). The coated samples will be referred to as 4AIF_LLS, 8AIF_LLS, and 16AIF_LLS to indicate the number of AlF3 cycles used during the coating process. The uncoated sample will be referred to as LLS-baseline. The uncycled, coated cathode (4AIF_LLS) by TEM (Fig. 1) was analyzed to determine the quality of the ALD coating and to inspect the condition of the cathode surface before electrochemical cycling. First, HAADF imaging reveals a surface layer (SL) \sim 1 nm thick that is distinctly different from the bulk structure (Fig. 1a). A SL of the same size was also observed on each of the coated samples and on the LLS-baseline cathode (not shown). Annular-bright-field (ABF) STEM imaging (Fig. 1b), uses the low-angle elastically scattered

electrons near the optical axis and is primarily regarded as a phase-contrast imaging mode. Therefore, the difference in contrast of the *SL* observed in Fig. 1b indicates a different phase to the layered area beneath. ²⁶ The surface phase was confirmed as spinel (Fd-3m) on the basis of the TEM analysis shown in Fig. S1.

Furthermore, HAADF imaging (Fig. 1a) also reveals the coating is nearly invisible, signifying that the ALD coating is made up of mostly light elements. The use of ABF imaging, which is sensitive to light elements, confirms the presence of an amorphous, ~2.5-nmthick coating (Fig. 1b). The observed coating thickness is higher than the expected thickness of ~ 1.4 nm for the bilayer coating of AlW_xF_y (1 nm) and 4AlF₃ (0.4 nm). The difference from the expected thickness may be due, in part, to the surface "roughness" of the electrode laminates, while the growth rates were measured on flat substrate surfaces (Si). EDS analysis of the primary particle shown in Figs. 1a and 1b reveals a homogenous distribution of Ni, Mn, and Co throughout the particle (Figs. 1c-1e). Additionally, the presence of W (Fig. 1f) was observed throughout the particle, while enrichment of Al (Fig. 1g) was observed on the outer layer, as expected from the coating procedure, in which deposition of AlF₃ was the last step. Similar analyses were carried out on various particles for the coated samples, and the results were comparable (i.e., SL size and coating composition), apart from thickness of the coating, which was intentionally varied by increasing the number of AlF₃ cycles used during the coating process.

Electrochemical testing.—The performance of the four samples (i.e., one uncoated and three coated) was tested vs graphite anodes. The protocol consisted of an activation cycle between 4.5 and 2.0 V. followed by four cycles between 4.4 and 2.5 V, all at C/10. Each cycle thereafter included a 3-h hold at the top of charge (4.4 V), which probes the instability of the surface of the oxide with respect to damaging secondary reactions (e.g., electrolyte decomposition, surface reconstruction, and/or transition metal dissolution). If the cathode surface is prone to undesirable reactions, the degradation of the cell is accelerated in comparison to a cathode with a stable surface. Figure 2a shows the results for this targeted protocol. Each coated sample delivered a lower first-cycle charge capacity when compared to the baseline sample (LLS-baseline: 256 mAh g⁻¹, 4AlF_LLS: 244 mAh g⁻¹, 8AlF_LLS: 237 mAh g⁻¹ and 16AlF_LLS: 240 mAh g⁻¹). On the initial discharge, the LLS-baseline sample delivered 215 mAh g⁻¹, while the coated samples delivered sequentially lower capacity as the coating thickness increased (i.e., 195, 180, and 175 mAh g⁻¹) suggesting that a thinner coating is optimal for achieving higher capacity. The increasing amount of AlF₃, which is known to be insulating, may be lowering the reversible capacity. Despite delivering a higher initial capacity, the LLS-baseline sample deteriorated rapidly; in contrast, each of the coated samples, irrespective of coating thickness, delivered a higher capacity by the 30th cycle. The uncoated sample reached end of life (defined as 80% of the second-cycle capacity) by the 35th cycle, amounting to \sim 70 h at

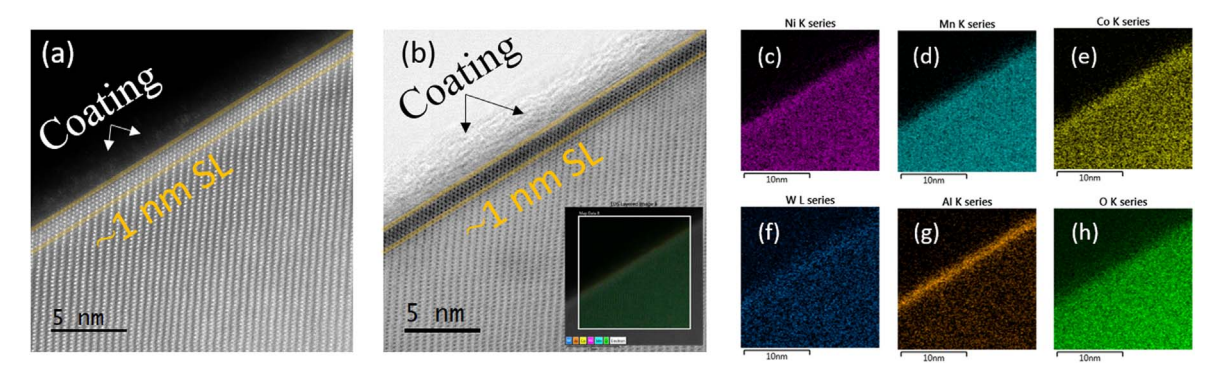


Figure 1. All images are of 4AIF_LLS and are representative of the coated samples. (a) high-angle annular dark-field (HAADF) and (b) annular-bright-field (ABF) images and STEM-EDS mapping displaying the distribution of (c) Ni, (d) Mn, (e) Co, (f) W, (g) Al, and (h) O on a single particle.

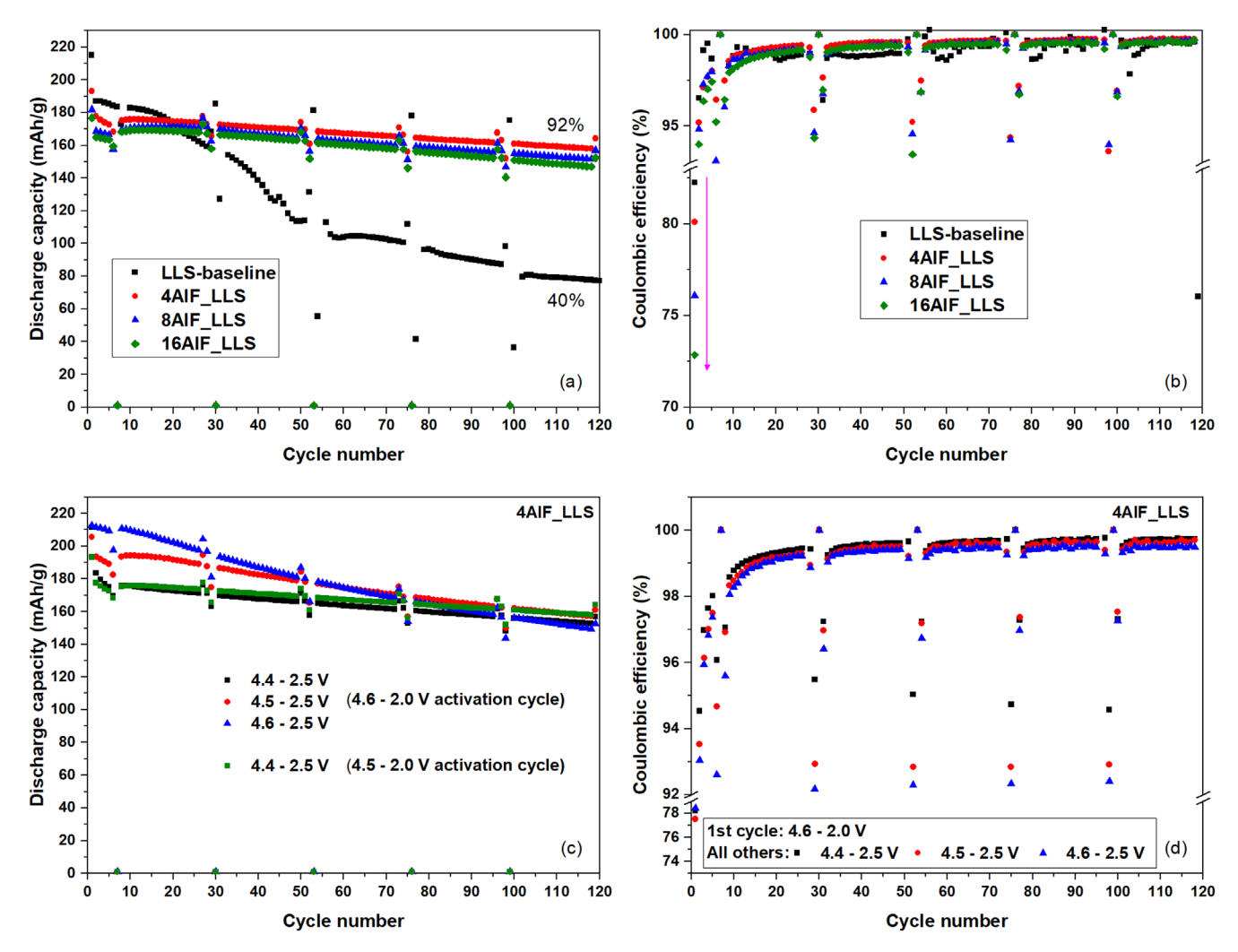


Figure 2. (a) Discharge capacity and (b) C.E. vs cycle number of LLS-baseline, 4AIF_LLS and 16AIF_LLS cathodes. All cycling was done at 30 ° C. A first-cycle activation was carried out between 4.5 and 2.0 V. All other cycles were between 4.4 and 2.5 V. (c) Discharge capacity and (d) C.E. vs cycle number of 4AIF_LLS using a different upper cutoff voltage during activation (4.5 and 4.6 V, respectively), followed by continuous cycling as labeled in (c) and (d).

high voltage (i.e., 4.4 V vs graphite). In contrast, the coated samples all retained >89% capacity at the end of the 120-cycle protocol, approaching 300 h above 4.4 V, with the thinnest coating demonstrating the highest capacity retention (92%) of all samples. Figure 2b shows the accompanying coulombic efficiency (C.E.) for each of the samples. The first-cycle efficiency was highest for LLS-baseline (84%) and decreased as the thickness of the coating increased (4AIF_LLS: 80%, 8AIF_LLS: 76%, and 16AIF_LLS: 73%). The C.E. of LLS-baseline was, on average, lower than that of the coated samples during the cycling protocol and showed somewhat erratic behavior. All coated samples, however, showed smooth C.E. curves over the time on test, with increasing C.E. as the coating thicknesses decreased.

Because the extent of activation that occurs during the first cycle is known to affect the electrochemical performance of Mn-rich cathodes, and because the LLS-baseline sample underwent slightly higher activation (i.e., based on first-cycle charge capacity) than the coated samples, the performance of the 4AIF_LLS sample was tested using a higher upper cutoff voltage (4.6 V) to initiate greater activation during the first cycle. Figure 2c shows that when the upper cutoff voltage is raised to 4.6 V (instead of 4.5 V) for the 4AIF_LLS sample, the first-cycle discharge capacity increases to 211 mAh g⁻¹. Yet, decreasing the upper cutoff voltage to 4.4 V on subsequent cycles results in a similar capacity as the 4.5 V activation, revealing that the additional Li extracted during the higher voltage "activation"

remains inactive during subsequent cycles. This result suggests that the higher voltage activation has done little to damage the oxide and that a wider voltage window is necessary to continue cycling additional lithium, as presented below. Additionally, the capacity retention is very similar for both protocols when cycled between 4.4 and 2.5 V, irrespective of the activation. The capacity retention of the 4AIF_LLS sample was further tested by opening the voltage window during extended cycling to 4.5-2.5 V and 4.6-2.5 V (Fig. 2c). The first-cycle capacity was similar whenever the activation was between 4.6 and 2.5 V, but the capacity during the extended cycle increased as the voltage window was opened. However, the higher capacity achieved by using an upper cutoff voltage of 4.5 V or 4.6 V came at the expense of faster capacity fade. Despite the higher capacity loss experienced by the 4AlF_LLS when cycled at higher voltage, the capacity retention was still far superior to that of the uncoated sample (Fig. 2a) cycled to a lower voltage. These results suggest the bilayer coating can limit unwanted reactions at the cathode surface and, therefore, improve the capacity retention. Post-analysis of the cathodes and anodes is discussed further in a later section.

The area-specific impedance (ASI) of each sample was collected at various stages of testing (i.e., after every 23 ageing cycles), as shown in Fig. 3. Since impedance growth in full cells (vs graphite) is governed by the cathode–electrolyte interface, ²⁷ the ASI data provide a glimpse into the changing surface of the cathode upon

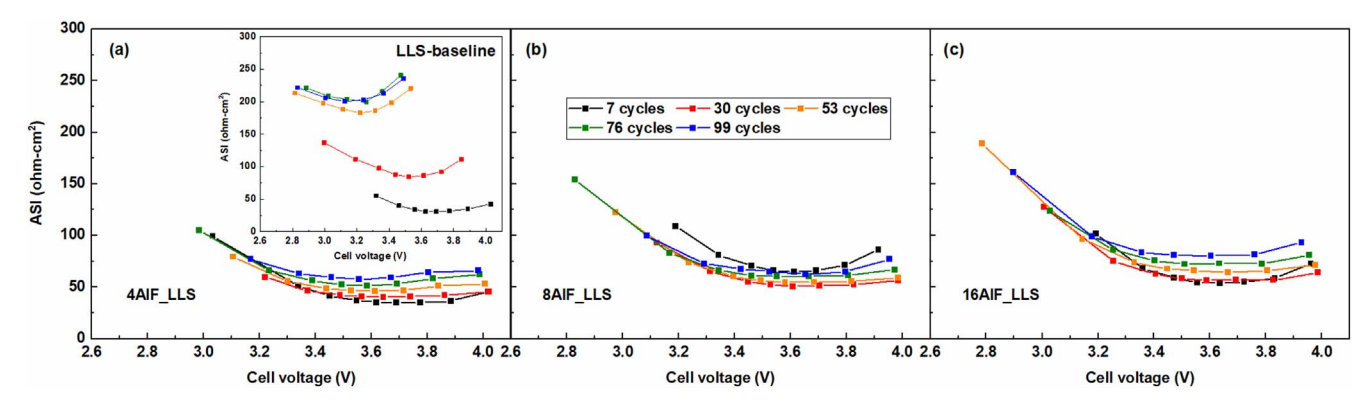


Figure 3. Area-specific impedance as a function of voltage for (a) 4AIF_LLS, (b) 8AIF_LLS, (c) 16AIF_LLS, and LLS-baseline (a, inset). Each continuous line with symbols represents one HPPC collected at the indicated cycle shown in the legend.

extended cycling and, therefore, the data are a measure of the effectiveness of the various ALD coatings to limit side reactions that inhibit fast charge transfer across the interface. Each of the curves in Fig. 3 illustrates the discharge impedance of the cycle shown in the legend. The lowest impedance during each cycle is expected to occur at mid-SOC, giving a U-shape to each curve. The initial ASI of LLS-baseline (Fig. 3a, inset) and 4AIF_LLS were similar (~50 ohm-cm²), but the untreated baseline sample experienced a much larger *rise* in impedance (~225 ohm-cm²) compared to 4AIF_LLS (~75 ohm-cm²) over the cell life. Although the impedance *rise* was similar for all three coatings, the *initial* impedance (7th cycle) was higher as the coating thickness increased (Figs. 3b–3c), which resulted in 4AIF_LLS exhibiting the lowest *final* ASI. Both the capacity retention and impedance results suggest that a thinner coating of AIF₃ is superior to a thicker one.

Post-analysis of cycled anode and cathode.—A major source of capacity fade (actual loss of cyclable Li) in transition metal-oxide// graphite cells is the loss of Li ions due to reactions at the anode.²⁷ The "trapping" of lithium has been shown to correlate with the dissolution of transition metals from the cathode and their ensuing deposition on the anode, ^{28,29} especially in the case of manganese. Hence, an analysis of the cycled graphite used in full cells paired against either LLS-baseline or 4AIF_LLS cathodes was carried out (Fig. 4). Each anode contained two visibly distinct regions, one darker and one lighter. Each region is labeled with a number and colored box in the SEM images (Figs. 4a and 4b). The corresponding (by color) EDS spectrum is shown in Figs 4c and 4d, respectively. The darker region for LLS-baseline (red box, labeled 1) is the underlying graphite, as the C peak is much more intense than the spectrum for the lighter region (green box, labeled 2). Markedly, the lighter region contains relatively high levels of electrolyte decomposition products (F and P), along with evidence of transition metal deposition (inset of Fig. 4c; Mn, Ni, and Co). On the other hand, the differences between the two regions on 4AlF_LLS anode (Fig. 4b) are not as drastic as those observed for the anode paired with the LLS-baseline sample. For instance, the amount of transition metals (Mn, Ni and Co, inset of Fig. 4d) deposited on the 4AIF_LLS anode is substantially lower by comparison (note that different scales are used for the insets of Figs. 4c and 4d). In addition, the intensity of the C peak for both regions are similar, suggesting the lighter region on 4AlF_LLS is thinner, allowing the underlying graphite to be observed with no obstruction of the signal by decomposition products. Indeed, a visual comparison of the lighter regions (Figs. 4a and 4b) suggests the amount of decomposition product on the LLS-baseline anode is thicker (Fig. 4a: see the 'edges that show the underlying carbon and top layer of decomposition product) than what is found on the anode paired against 4AlF_LLS (Fig. 4b). The EDS results align well with the electrochemical performance of the samples, confirming the effectiveness of the ALD coating in suppressing transition metal dissolution during cycling. It is

interesting to note that although W was clearly identified at the anode, the sample with this coating performed extremely well. This result contrasts with previous reports citing W dissolution and deposition as the main source of capacity fade for coatings containing W.³¹ This suggests that the chemical nature of the W from the bilayer ALD coating is rather benign, as deposited, at the graphite surface in working cells. More work is needed to understand the details but is beyond the scope of this paper.

The higher levels of deposited transition metals on the anode paired against the untreated baseline cell(s) suggest the surface of the untreated cathode underwent greater transformation during cycling. Therefore, TEM analysis was done on LLS-baseline and 4AlF_LLS after cycling (i.e., ~120 cycles) was completed for comparison. A visual inspection of the image of LLS-baseline after cycling (Fig. 5a) shows uniform layers of transition metals in the bulk of the cathode. As the edge of the crystal is reached, a surface reconstruction layer (SRL) between 2 and 3 nm thick can be observed, where transition metal ions are also present in the interslab space between the layers. Considering that the surface layer of the uncycled LLS-baseline was \sim 1 nm to begin with, the cycling caused \sim 1–2 nm of reconstruction on the surface of the untreated cathode. On the other hand, the surface of 4AlF_LLS after cycling (Fig. 5b) appears unchanged $(\sim 1 \text{ nm})$ from the uncycled cathode. The TEM analysis of the cycled cathodes also support the EDS results, which show higher levels of transition metals on the anode paired against the uncoated electrode. The reconstructed layer is denser than the bulk and, ^{32,33} therefore, is likely also contributing to the high impedance rise in the cell paired against the untreated cathode. Furthermore, XPS data (see SI Figs. S3-S5) also support the conclusion that much less change occurs to the cathode surface protected with the bilayer coating.

In addition, graphite electrodes cycled against uncoated, Mn-rich electrodes, where significant Mn dissolution can occur, can also lead to poor performance of graphite anodes, as reported in Ref. 34. As such, contributions from the metal oxide are not the only source of impedance rise in the presence of significant transition metal dissolution and deposition at the anode.

For NMC-type oxides, especially those rich in Ni, Mn dissolution is much less of an issue on a per-cycle basis. However, impedance rise with cycling is a concern, particularly as the Ni content increases. The bilayer coating was also applied to NMC-532, NMC-622, and NMC-811 electrodes, and the electrochemical performance was compared to the uncoated NMCs. The thickness of the first ALD layer (1 nm of AlW_xF_y) in the bilayer coating was the same used for the LLS electrodes. The second layer (AlF₃) was deposited using 8 cycles and, therefore, the coated NMC electrodes are referred to as 8AlF_NMC-532, 8AlF_NMC-622, and 8AlF_NMC-811. The same aggressive protocol, using 3-h holds at the top of charge, was used for testing except the cycling and HPPC was collected between 4.4–3.0 V (vs graphite). The coating had little to no effect on the capacity delivered by each of the NMC chemistries, as both coated and uncoated samples delivered similar

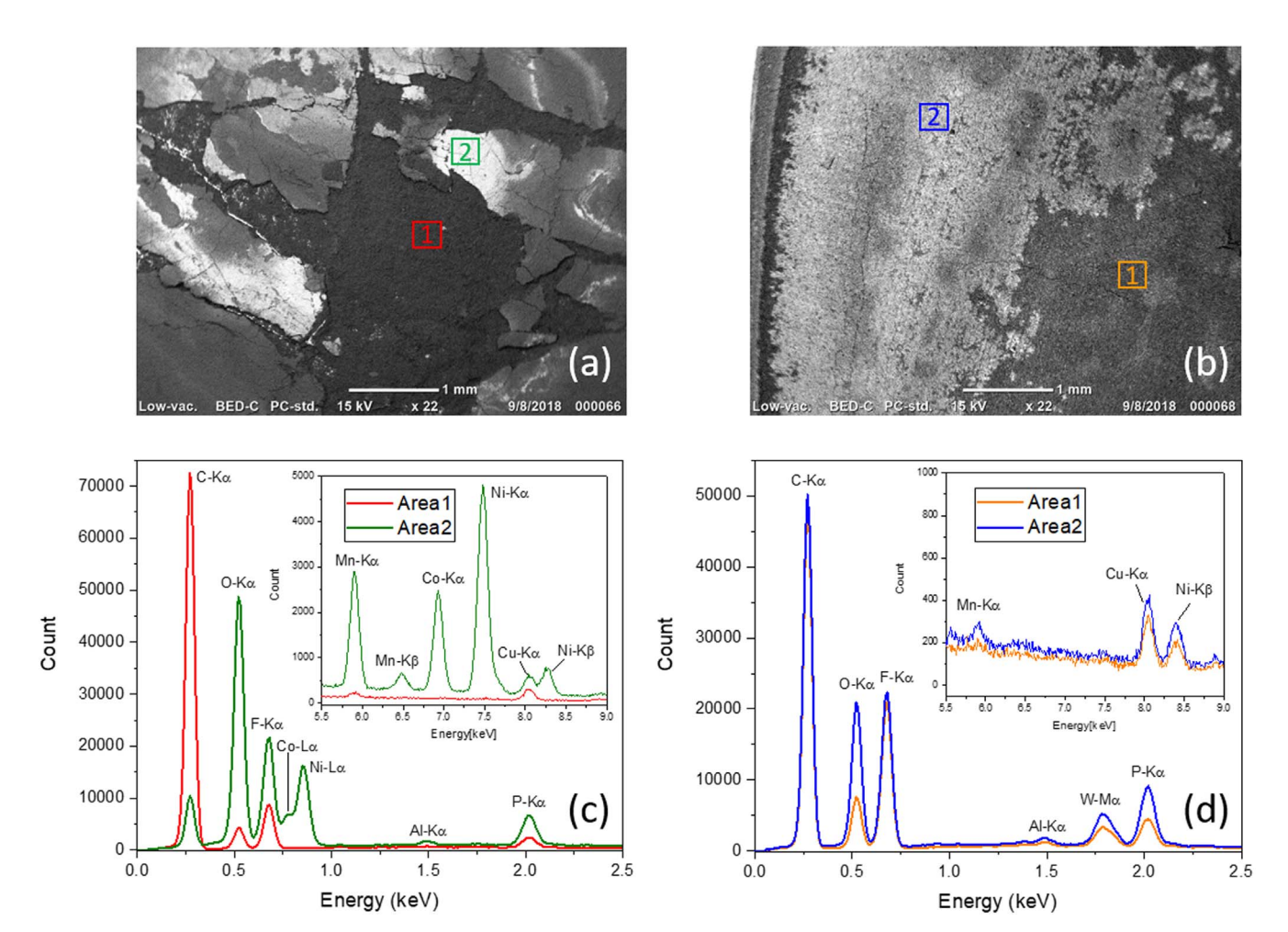


Figure 4. Post-cycling analysis (SEM, top; EDS, bottom) of graphite anodes used in full cells paired against (a), (c) LLS-baseline and (b), (d) 4AIF_LLS. The cycling protocol is described in the Experimental section. Each SEM figure (top) shows two colored (and numbered) boxes showing two visibly different regions on the anodes. The color of each box is coordinated to the color of the EDS spectrum (bottom) collected on each region. The *y*-axis scales are different in spectrum.

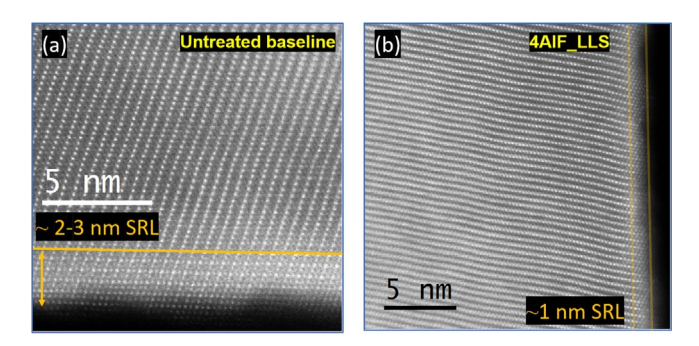


Figure 5. Atomic-resolution HAADF images of harvested electrodes after electrochemical cycling was complete: (a) LLS-baseline and (b) 4AlF_LLS.

capacities (Fig. S6). These results reinforce the idea that coatings, and surface treatments in general, need to be optimized for the surface chemistry of each cathode of interest. In addition, the capacity fade was also very similar between the coated and uncoated NMC samples. This behavior is understandable because much less Mn dissolution is expected from these compositions, which in turn would lower the rate of lithium trapping at the anode.

The uncoated NMC electrodes did, however, experience significant impedance rise over the course of the protocol (Figs. 6a–6c): the impedance rise drastically increased as the Ni content increased from 532 to 811. On the contrary, the 8AIF_NMC-532 and

8AIF_NMC-622 samples (Figs. 6d and 6e) exhibited negligible impedance rise over the course of cycling, and the impedance rise for the 8AIF_NMC-811 sample (Fig. 6f) was mitigated by ~80% over the 120 high-voltage cycles. It is known that the major source of impedance rise for Ni-based chemistries is changes at the oxide surface (metal reduction, oxygen loss, reconstruction, interphase) even in the absence of significant capacity loss (i.e., loss of Li sites within the bulk of the oxide). Therefore, the results clearly indicate that the coating is mitigating factors that impede Li diffusion, especially as the Ni content goes up. Obviously, coatings need to be optimized for cathode surface composition (e.g., Li-rich/Mn-rich, vs layered Ni-rich), but the multilayer strategy looks promising in terms of the diversity it offers (i.e., many ALD precursors available).

Conclusions

This work introduces a new strategy for stabilizing electrode materials that utilizes multilayer films deposited by atomic layer deposition. In a simple but novel example, bilayer AlW_xF_y/AlF₃ coatings were applied to Mn-rich and Ni-rich cathodes, which were subjected to prolonged exposure to high-voltage electrochemical cycling in cells using graphite anodes. For Mn-rich electrodes, the coatings offered substantial benefits in terms of high-voltage stability; in particular, the effects of Mn dissolution on capacity fade were drastically reduced. Furthermore, impedance rise with cycling was virtually eliminated in these cells. Data from TEM, EDS, and XPS confirmed that the surfaces of Mn-rich electrodes underwent less change (e.g., dissolution/reconstruction) during

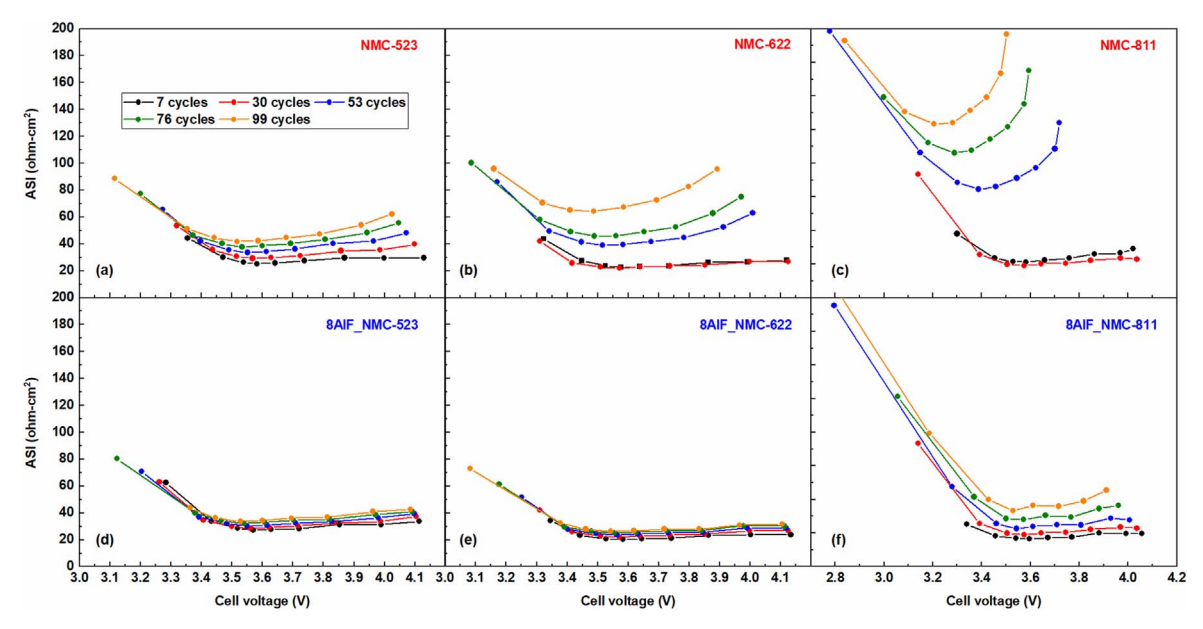


Figure 6. Area-specific impedance as a function of voltage for (a) uncoated NMC-523, (b) uncoated NMC-622, (c) uncoated NMC-811, (d) 8AIF_NMC-523, (e) 8AIF_NMC-622, and (f) 8AIF_NMC-811. Each continuous line with symbols represents one HPPC collected at the indicated cycle shown in the legend.

cycling than those of uncoated electrodes. Similar tests on a series of NMC electrodes with increasing Ni content showed that the multilayer coating was capable of significantly reducing impedance rise under high-voltage cycling, especially in the most Ni-rich composi-

The results presented in this study reveal exciting opportunities for the development of robust electrochemical interfaces. The wide variety of available ALD precursors, as well as the versatility of deposition conditions (e.g., substrates, time, cycles, temperature, multiple precursors), bodes well for the concept of multilayer films and the ability to tune the properties of complex interfaces. This strategy continues to be developed at Argonne National Laboratory for advanced lithium-ion and "beyond lithium-ion" technologies, such as solid-state batteries.

Acknowledgments

Argonne National Laboratory's work was supported by the U.S. Department of Energy (DOE) Office of Science laboratory under Contract No. DE-AC02-06CH11357. The U.S. Government retains for itself, and others acting on its behalf, a paid-up, nonexclusive, irrevocable worldwide license in said article to reproduce, prepare derivative works, distribute copies to the public, and perform publicly and display publicly, by or on behalf of the Government. The Department of Energy will provide public access to these results of federally sponsored research in accordance with the DOE Public Access Plan. http://energy.gov/downloads/doe-public-access-plan. This research used resources of the Advanced Photon Source, a DOE Office of Science User Facility operated for the DOE Office of Science by Argonne National Laboratory under Contract No. DE-AC02-06CH11357. R. Shahbazian-Yassar acknowledges the financial support from National Science Foundation (CBET-1805938).

ORCID

Arturo Gutierrez https://orcid.org/0000-0002-2899-3089 Reza Shahbazian-Yassar https://orcid.org/0000-0001-5787-1630

References

- 1. V. T. O. U. S. Department of Energy, Annual Merit Review Report (2018).
- 2. Z. H. Lu, L. Y. Beaulieu, R. A. Donaberger, C. L. Thomas, and J. R. Dahn, J. Electrochem. Soc., 149, A778 (2002).
- 3. M. M. Thackeray, C. S. Johnson, J. T. Vaughey, N. Li, and S. A. Hackney, J. Mater. Chem., 15, 2257 (2005).

- 4. M. M. Thackeray et al., Sustain Energ Fuels, 2, 1375 (2018).
- 5. J. R. Croy, M. Balasubramanian, K. G. Gallagher, and A. K. Burrell, Acc. Chem. Res., 48, 2813 (2015).
- J. R. Croy, K. G. Gallagher, M. Balasubramanian, B. R. Long, and M. M. Thackeray, J. Electrochem. Soc., 161, A318 (2014).
- J. R. Croy, D. Kim, M. Balasubramanian, K. Gallagher, S.-H. Kang, and M. M. Thackeray, J. Electrochem. Soc., 159, A781 (2012).
- D. Kim, G. Sandi, J. R. Croy, K. G. Gallagher, S. H. Kang, E. Lee, M. D. Slater, C. S. Johnson, and M. M. Thackeray, J. Electrochem. Soc., 160, A31 (2013).
- 9. B. R. Long, J. R. Croy, J. S. Park, J. G. Wen, D. J. Miller, and M. M. Thackeray, J. Electrochem. Soc., 161, A2160 (2014).
- 10. J. R. Croy, J. S. Park, Y. Shin, B. T. Yonemoto, M. Balasubramanian, B. R. Long, Y. Ren, and M. M. Thackeray, J. Power Sources, 334, 213 (2016).
- S. M. George, *Chem. Rev.*, **110**, 111 (2010).
 I. D. Scott, Y. S. Jung, A. S. Cavanagh, Y. Yan, A. C. Dillon, S. M. George, and S.-H. Lee, Nano Lett., 11, 414 (2011).
- 13. H.-M. Cheng, F.-M. Wang, J. P. Chu, R. Santhanam, J. Rick, and S.-C. Lo, The Journal of Physical Chemistry C, 116, 7629 (2012).
- 14. A. M. Wise et al., Chem. Mater., 27, 6146 (2015).
- 15. J. Ahn, E. K. Jang, S. Yoon, S.-J. Lee, S.-J. Sung, D.-H. Kim, and K. Y. Cho, Appl. Surf. Sci., 484, 701 (2019).
- 16. M. R. Laskar, D. H. K. Jackson, S. Xu, R. J. Hamers, D. Morgan, and T. F. Kuech, ACS Appl. Mater. Interfaces, 9, 11231 (2017).
- 17. P. F. Yan, J. M. Zheng, X. F. Zhang, R. Xu, K. Amine, J. Xiao, J. G. Zhang, and C. M. Wang, Chem. Mater., 28, 857 (2016).
- 18. C. C. Wang, J. W. Ling, Y. H. Yu, K. H. Lai, K. F. Chiu, and C. C. Kei, Acs Sustain Chem Eng. 6, 16941 (2018).
- 19. J. Xie et al., *Acs Nano*, **11**, 7019 (2017).
- 20. Y. Xiao, L. J. Miara, Y. Wang, and G. Ceder, Joule, 3, 1252 (2019).
- 21. T. Oi, K. Miyauchi, and K. Uehara, J. Appl. Phys., 53, 1823 (1982).
- 22. J. S. Park, A. U. Mane, J. W. Elam, and J. R. Croy, Chem. Mater., 27, 1917 (2015).
- 23. A. U. Mane and J. W. Elam, Chem. Vap. Deposition, 19, 186 (2013).
- 24. B. R. Long et al., J. Electrochem. Soc., 163, A2999 (2016).
- 25. Y. Lee, J. W. DuMont, A. S. Cavanagh, and S. M. George, The Journal of Physical Chemistry C, 119, 14185 (2015).
- 26. T. Seki, N. Takanashi, and E. Abe, Ultramicroscopy, 194, 193 (2018).
- 27. J. A. Gilbert, J. Bareno, T. Spila, S. E. Trask, D. J. Miller, B. J. Polzin, A. N. Jansen, and D. P. Abraham, J. Electrochem. Soc., 164, A6054 (2017). 28. N. P. W. Pieczonka, Z. Liu, P. Lu, K. L. Olson, J. Moote, B. R. Powell, and J.-
- H. Kim, The Journal of Physical Chemistry C, 117, 15947 (2013). 29. A. Jarry, S. Gottis, Y.-S. Yu, J. Roque-Rosell, C. Kim, J. Cabana, J. Kerr, and
- R. Kostecki, J. Am. Chem. Soc., 137, 3533 (2015). 30. J. A. Gilbert, I. A. Shkrob, and D. P. Abraham, J. Electrochem. Soc., 164, A389
- (2017).31. X. Yang, Z. Zuo, H. Wang, Q. Chen, H. Zhang, Z. Huang, B. Wu, and H. Zhou,
- Electrochim. Acta, 180, 604 (2015). 32. N. Tran, L. Croguennec, M. Ménétrier, F. Weill, P. Biensan, C. Jordy, and
- C. Delmas, Chem. Mater., 20, 4815 (2008). A. Boulineau, L. Simonin, J.-F. Colin, C. Bourbon, and S. Patoux, Nano Lett., 13,
- 3857 (2013).
- A. Gutierrez, M. He, B. T. Yonemoto, Z. Yang, J. Wang, H. M. Meyer, M. M. Thackeray, and J. R. Croy, J. Electrochem. Soc., 166, A3896 (2019).